Proceedings of ENCIT 2016
Copyright © 2016 by ABCM

16th Brazilian Congress of Thermal Sciences and Engineering
November 07-10th, 2016, Vitória, ES, Brazil

A STUDY OF ATMOSPHERIC RE-ENTRY FLOWS THROUGH THE COMPARISON OF RANS, DSMC AND EXPERIMENTAL DATA

Daniel Ferreira Viotti, danielviotti@gmail.com[1]
Ruan Ramon Penha dos Passos Pereira, passosruan@gmail.com[2]
Vincent Casseau, vincent.casseau@strath.ac.uk[3]
Daniel Espinoza, daniel.espinoza.vasquez@gmail.com[3]
Rodrigo C. Palharini, palharini.rc@gmail.com[2]
João Luiz F. Azevedo, joaoluiz.azevedo@gmail.com[2]

[1]Instituto Tecnológico de Aeronáutica, DCTA/ITA, São José dos Campos, SP, 12228-904, Brazil
[2]Instituto de Aeronáutica e Espaço, DCTA/IAE/ALA, São José dos Campos, SP, 12228-904, Brazil
[3]James Weir Fluids Laboratory, University of Strathclyde, Glasgow, G1 1XJ, UK

Abstract: *The Aerodynamic Division of IAE is developing a computational tool capable of solving the hypersonic flow in atmospheric re-entry conditions. This tool comprises a Reynolds-averaged Navier-Stokes (RANS) code for altitudes in which the Knudsen number is sufficiently low such and a Direct Simulation Monte Carlo (DSMC) code for high altitudes. The main objective of the present study is to compare the RANS code results with experimental data and with results obtained from the DSMC approach at intermediate altitudes in which the Knudsen number is sufficiently low that the continuum hypothesis is valid. The obtained results show concordance in the regions of low local Knudsen number and overestimate the heat flux in the regions with high degree of rarefaction.*

Keywords: *Aerothermodynamic, Atmospheric Re-entry , RANS, DSMC*

1. INTRODUCTION

The atmospheric re-entry of a space vehicle is one of the most critical phase of the vehicle trajectory. During the reentry, the spacecraft is exposed to high Mach numbers and the high temperatures conditions. Such conditions requires the the development of experimental and numerical techniques capable of accurately predict the vehicle's aerothermodynamics. More importantly, is the use of these tools for the development of reliable thermal protection systems to assure the integrity of the experiments and human life in case of manned missions.

Recently, the Instituto de Aeronáutica e Espaço (IAE) has been developing a sub-orbital platform flight called SARA, acronym of Satélite de Reentrada Atmosférica, with the objective of performing experiments in microgravity environment. Aerothermodynamic analyses are required in order to calculate the aerodynamic forces and the heat flux acting on the capsule to guarantee its survivability during the harsh reentry phase. In doing so, the Aerodynamic Division of IAE is developing a computational tool capable of solving the hypersonic flow in atmospheric re-entry conditions.

The main goal of this paper is to present the preliminary results obtained using a *in house* Computational Fluid Dynamics (CFD) code based on the Reynolds-averaged Navier-Stokes (RANS) formulation for a non-reacting flow over a 70^o blunted cone. The computations are compared with numerical and experimental data available in the open literature. The computational tool used in the present work was developed by Scalabrin (2007) during his Ph.D. at the University of Michigan. This code passed through several modifications since it was developed and a carefully validation is necessary before its application in real engineering problems. Granted the similarity of the results, the tool is able to be applied in many cases of interest of the Institute.

2. THEORETICAL AND NUMERICAL FORMULATION

2.1 Mathematical Formulation

The RANS code of the present work is a viscous laminar code without turbulence model. The Navier-Stokes (N-S) conservation equations for the three-dimensional system can be write as

$$\frac{\partial Q}{\partial t} + \frac{\partial (E - E_v)}{\partial x} + \frac{\partial (F - F_v)}{\partial y} + \frac{\partial (G - G_v)}{\partial z} = 0\,. \tag{1}$$

The vector of conserved variables, Q, and the inviscid and viscous flux vectors in the x-direction are given, respectively, by

$$Q = \left\{ \begin{array}{c} \rho \\ \rho u \\ \rho v \\ \rho w \\ e \end{array} \right\}, \qquad E = \left\{ \begin{array}{c} \rho u \\ \rho u^2 + p \\ \rho u v \\ \rho u w \\ (e+p)u \end{array} \right\}, \qquad E_v = \left\{ \begin{array}{c} 0 \\ \tau_{xx} \\ \tau_{xy} \\ \tau_{xz} \\ \tau_{xx}u + \tau_{xy}v + \tau_{xz}w - q_x \end{array} \right\}. \tag{2}$$

In these expressions, ρ is the specie density, *u*, *v* and *w* are the bulk velocity components, *P* is the pressure, *e* the total energy, τ_{ij} the viscous stress components and q_x is the translational-rotational heat flux.

The viscous stress is assumed to be a Newtonian fluid and using Stokes's hypothesis is

$$\tau_{ij} = \mu\left(\frac{\partial u_j}{\partial x_i} + \frac{\partial u_i}{\partial x_j}\right) + \lambda\nabla\vec{u}\delta_{ij} \tag{3}$$

where μ is the coefficient of viscosity. The heat fluxes are modeled according do Fourier's law as

$$\vec{q} = -\kappa\nabla T \tag{4}$$

where κ is the the thermal conductivity coefficient. The thermodynamic properties are given by gas states equations by the perfect gas law

$$p = \rho RT \tag{5}$$

where *R* is the universal gas constant divided by the gas molecular mass. The total energy is given by

$$e = \rho Cv_{tr}T + \frac{1}{2}\rho(u^2 + v^2 + w^2) \tag{6}$$

where Cv_{tr} is the translational-rotational specific heat at constant volume. It is assumed that rotational and translational energy modes can be described by a single temperature T.

2.2 Numerical Method

The spatial integration uses the finite-volume method and the calculation of fluxes across cell faces. The inviscid component is calculated using the Flux Vector Splitting (FVS) and a centered scheme to calculate viscous component. The time integration is performed using an implicit method.

The set of equations in generic mesh cell, using the finite-volume method, is given by

$$V_{cl}\frac{\partial Q_{cl}}{\partial t} = -\sum_{j\in cl}(\vec{F}_j - \vec{F}_{dj})\cdot\vec{n}_j s_j = R_{cl} \tag{7}$$

where $\vec{F} = E\vec{i} + F\vec{j} + G\vec{k}$ is the the inviscid flux at the face, $\vec{F_d} = E_d\vec{i} + F_d\vec{j} + G_d\vec{k}$ is te diffusive flux at the face, V_{cl} is the volume of the *cl*-th cell, $\vec{n_j}$ is the normal vector to the *j*-th face pointing outward to the *cl*-th cell and s_j is the area of the *j*-th cell.

Using the homogeneous property of the inviscid flux vector (Scalabrin, 2007), the normal flux (F_n) at the *j*-th face can be written as

$$\vec{F}\cdot\vec{n} = F_n = \frac{dF_n}{dQ}Q = AQ \tag{8}$$

The matrix A is the matrix Jacobian of the inviscid flux, which can be diagonalized by its eigenvectors L and R as

$$A = L\Lambda R \tag{9}$$

or, separating into positive and negative parts as

$$A^+ = L\Lambda^+ R \; and \; A^- = L\Lambda^- R \tag{10}$$

The matrices Λ are the diagonal matrices of the eigenvalues of the Jacobian. The flux can be separated on a downstream and on an upstream flux in relation to the face orientation as

$$\vec{F}\cdot\vec{n} = F_j^+ + F_j^- = (A_{cl}^+ Q_{cl} + A_{cr}^- Q_{cr}). \tag{11}$$

The eigenvalues of the Jacobian are calculated by

$$\lambda^\pm = \frac{1}{2}(\lambda \pm \sqrt{\lambda^2 + \epsilon^2}) \tag{12}$$

where ϵ is a small number to correct sonic glitch, but it is also used to add numerical dissipation.

An implicit method is used for time integration. Implementing the Euler backward for the Eq. (6),

$$\frac{V_{cl}}{\Delta t}\Delta Q_{cl}^n = [-\sum_{j\in cl}(F_{n,j} - F_{dn,j})s_j]^{n+1} = R_{cl}^{n+1} \tag{13}$$

where R_{cl}^{n+1} is the residue at the cl-th cell. Linearizing the residue at time $n+1$ and using the FSV, the system of equations to be solved can be written as

$$M_{cl}\Delta Q_{cl}^{n} + \sum_{j\in cl} N_j^- \Delta Q_{cr,j}^{n} = R_{cl}^{n} \tag{14}$$

where

$$N_j^- = (A_{j-}^- - B_{j-}^-)s_j \tag{15}$$

$$N_j^+ = (A_{j+}^+ - B_{j+}^+)s_j \tag{16}$$

and

$$M_{cl} = \frac{V_{cl}}{\Delta t} + \sum_{j\in cl} N_j^+. \tag{17}$$

3. SIMULATION TEST CASES

Hypersonic flows simulations were performed over a a 70° blunted cone and the freestream condition a those obtained in the CNRS wind tunnel (Allegre *et al.*, 1997). A schematic to the geometry used the experiments is shown in Fig. 1(b) and the freestream used in the present work is illustrated in Table 1 (Moss *et al.*, 1993). From Fig. 1(b), the s is the distance around the surface of the probe beginning at the stagnation point. The blunted cone represents the heat shield of a re-entry planetary probe with $R_b = 5cm$. Two flight conditions were simulated (Tab. 1) with the same nominal Mach number and temperature, but at different Knudsen number. The probe was tested in the wind tunnel with a very low temperature toward to avoid any chemical reactions. The composition of the gas is pure molecular nitrogen N_2.

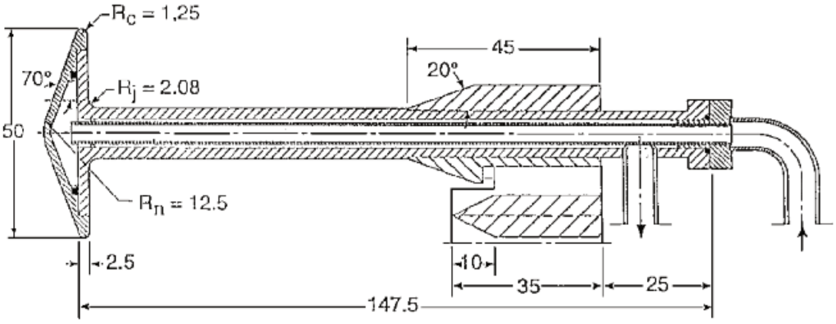

(a) Wind tunnel model

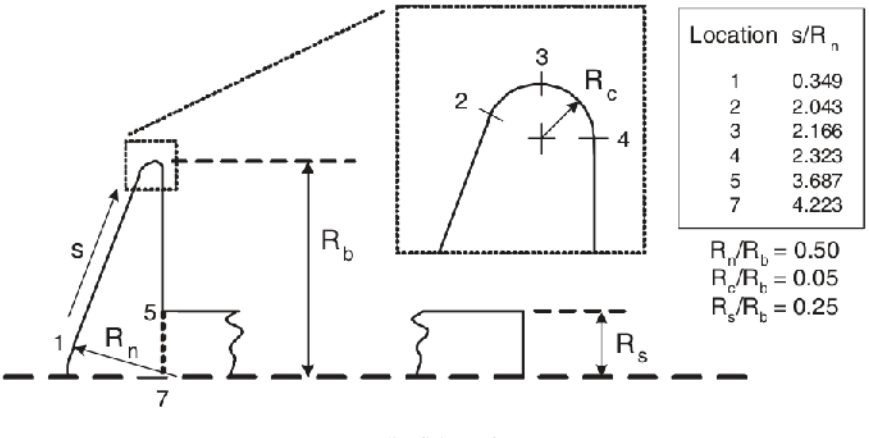

Location	s/Rn
1	0.349
2	2.043
3	2.166
4	2.323
5	3.687
7	4.223

(b) Schematic

Figure 1: Planetary probe geometry

Tabela 1: **Experimental flow conditions for the planetary probe configurations**

Case	M_∞	U_∞, m/s	ρ_∞, kg/m^3	T_∞, K	λ_∞, mm	T_ω, K	D_b, cm	Kn_g
2	20.0	1502,0	5.19×10^{-5}	14.0	0.54	300.0	5.0	0.01
3	20.5	1633,0	46.67×10^{-5}	15.0	0.54	300.0	5.0	0.001

The simulation results are compared with a wind tunnel experimental data (Moss *et al.*, 1993) and several other CFD codes. LeMANS and hyToFoam are RANS solvers. Monaco, DAC and dsmcFoam are DSMC solvers. The MPC is a hybrid solver composed by LeMANS and Monaco that switch between them depending on the local Knudsen number (Schwartzentruber *et al.*, 2008).

4. RESULTS AND DISCUSSION

4.1 Gradient-Length Knudsen Number

The Tab. 1 presents the global Knudsen number which is defined by the ratio of the mean-free path λ_∞ to a characteristic scale of interest l. However, Bird (1994) suggests that the local Knudsen number should be taken into account in order to determine in a more accurate manner the breakdown of the continuum theory. Because of the geometry and flow conditions, some rarefied regions mays appear and a particle based method is required to solve the flow at this regions. In this work the local Knudsen number is calculated using the concept of gradient-length Knudsen number given by

$$Kn_{GL-Q} = \frac{\lambda}{Q}|\nabla Q| \tag{18}$$

where Q is one of the quantities of interest: density ρ, temperature T and velocity magnitude $|V|$ (Schwartzentruber *et al.*, 2008). The maximum of Kn_{GL-Q} gives the local Knudsen number

$$Kn_{GL} = max(Kn_{GL-\rho}, Kn_{GL-T}, Kn_{GL-|V|}). \tag{19}$$

It is shown in Figure 2 the local Knudsen number (Kn_{GL}) for cases 2 and 3. In Fig. 2(b), the wake region has the local Knudsen number below 0.1 except for a small expansion region at the back of the shoulder where the Kn_{GL} reaches values bigger than 1. In the regions where $Kn_{GL} > 0.1$, the errors in the N-S formulation results are significant and the continuum model must be replaced by the molecular model for $Kn_{GL} > 0.2$ (Bird, 1994). Figure 2(a) shows the local Knudsen number for case 2 which is more rarefied than case 3, i.e., it has a bigger global Knudsen number Tab. 1. A great part of the the wake has $Kn_{GL} > 0.1$, especially in the red zone at the back of the probe, where $Kn_{GL} > 1$.

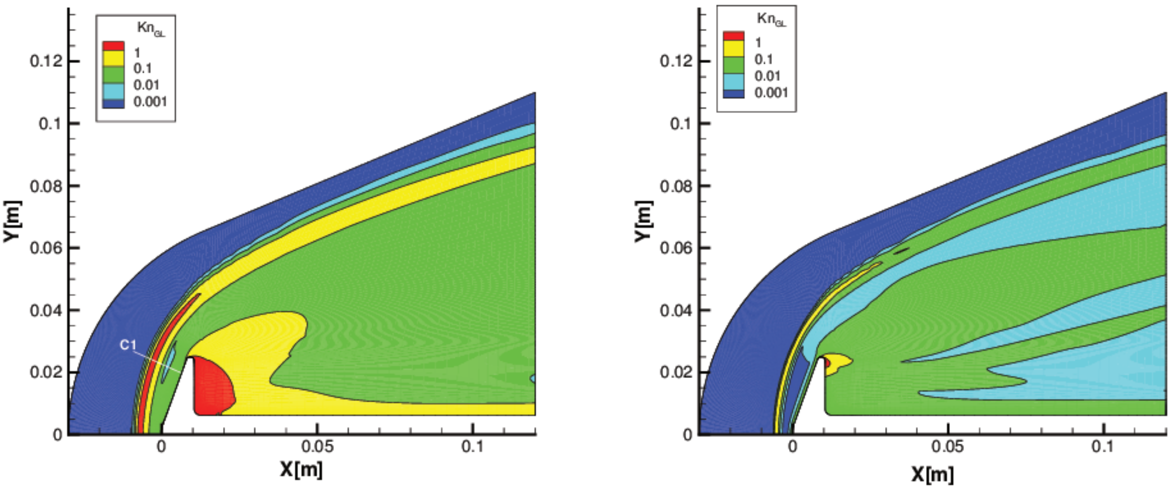

(a) Case 2

(b) Case 3

Figure 2: Gradient-length Knudsen Number for cases 2 and 3

4.2 Case 3

The probe was simulated in two dimensional axis-symmetrical squared structured-like grid (Fig. 3) and it was dimensioned in order to capture the shock wave inside the grid. At this case, the full geometry with the sting is considered. In Fig. 3(b) it is possible to see an amplified region of the grid near to the probe head. The mesh was refined at this region in order to capture the gradient of the properties close to the wall. This is necessary in order to capture more accurately the boundary layer and heat flux.

The streamlines and the Mach number distribution of case 3 are shown in Fig. 4(a). The temperate contour is shown in Fig. 4(b). According to these figures, the shock wave is well defined and the imposed exit boundary condition seems to have no impact on the downstream information propagation.

It is possible to see (Fig. 4(a)) the well resolved shock wave and the Mach number jump across the shock from supersonic to subsonic conditions in the region next to the stagnation point where the shock is approximately normal. In

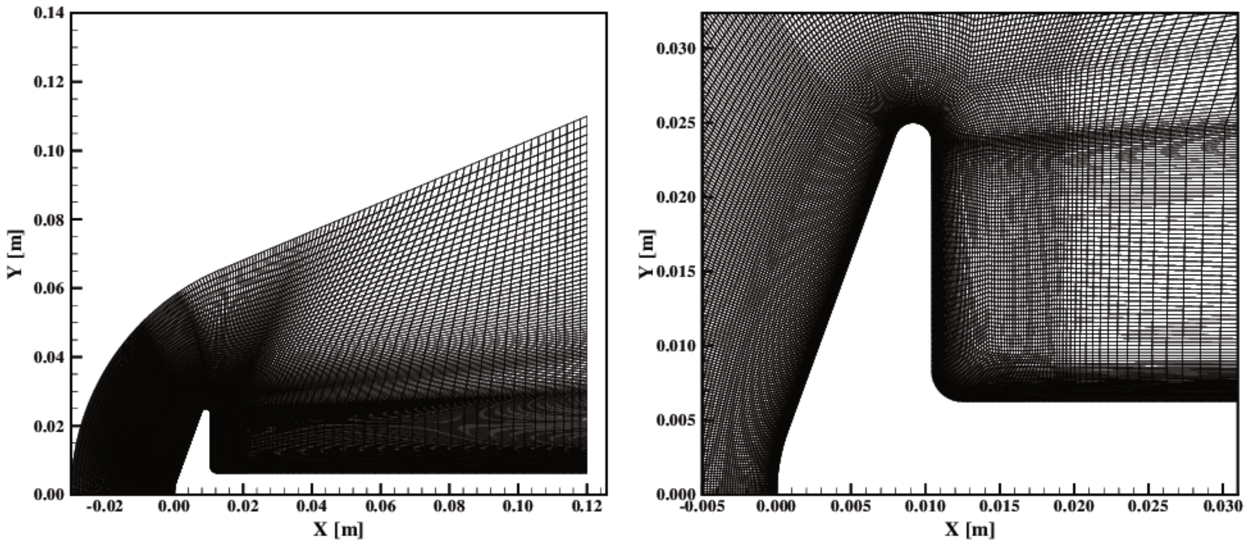

(a) Entire grid

(b) Zoom

Figure 3: Computational grid for case 3

the regions away from the stagnation point, the shock is oblique and the jump maintain the flow in supersonic conditions, although its drop is considerable. In addition, the expansion of the flow around the shoulder provides an increase of the Mach number as it is seen in Fig. 4(a). The streamlines show the formation of a vortex at the back of the blunted body and a very good agreement is noticed between the present simulation and the results shown by Moss *et al.* (1993) (Fig. 5).

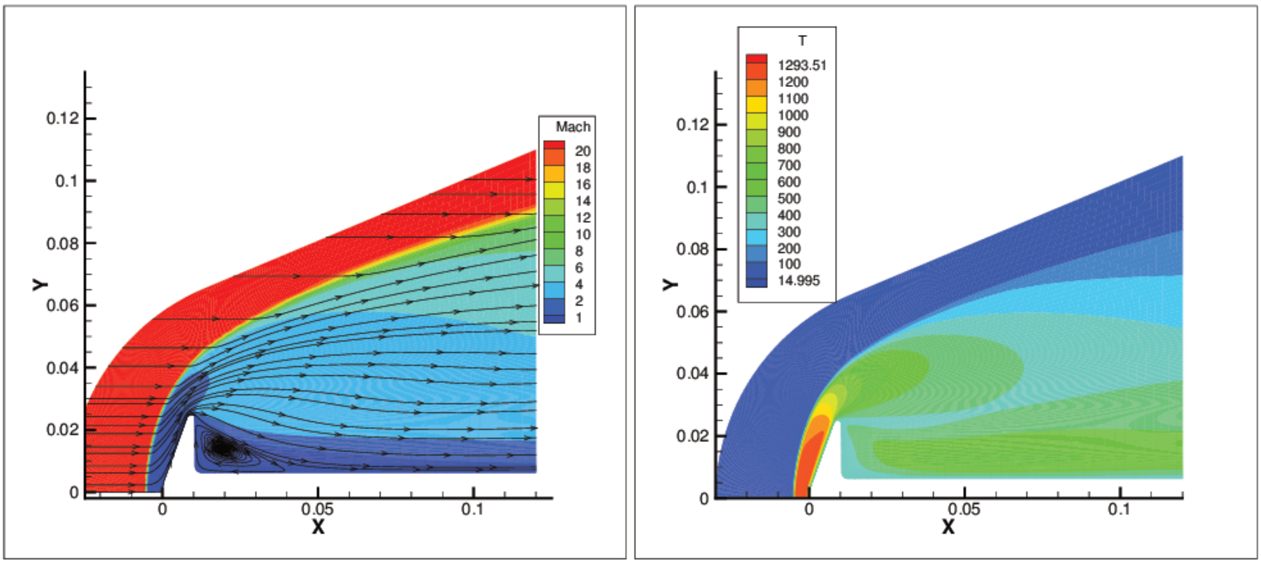

(a) Mach number

(b) Temperature

Figure 4: Simulation results

In the same way, the temperature distribution is influenced by the flow physics as explained in the paragraph above. There is a temperate jump across the shock wave from 15K to approximately 1200K close to the stagnation point. The results agree with the simulation hypothesis of cold gas flow because the maximum temperature achieved was 1293K. At this temperate no nitrogen chemical reactions will occur.

Figure 6 shows a comparison between the heat flux to the probe wall measured by different codes and compared with experimental data. There is a good agreement between the simulation results up to the shoulder region ($s/R_n \leq 2.0$). Furthermore, they predict the same peak heating at the stagnation point. After $s/R_n = 2.0$, the RANS solvers overestimate the magnitude of the heat flux comparing with those determined by the DSMC solvers. The divergence between RANS and DSMC at the shoulder is due to expansion region where the local Knudsen number became very high (Fig. 2(b)) for the N-S formulation. The continuum hypothesis, which is the basic hypothesis of the N-S formulation, is in the limit of validity which could produce results with no physical meaning. Along the most part of the heating shield, all the simulations predicted heating rates from 2-3 times larger than measured experimentally.

Concerning the pressure over the probe wall, the present simulation was compared with DAC (Moss *et al.*, 1993) (Fig. 6(b)). Despite the no agreement among the simulation results for the heat flux for $s/R_n \geq 2.0$, it is seen that the present simulation agree with the DAC solver result for the pressure loads. The heat flux is more dependent on the boundary

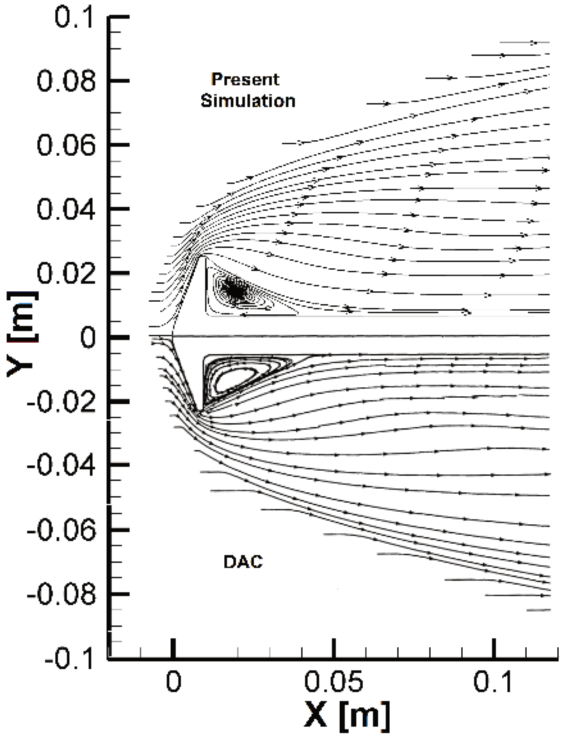

Figure 5: Vortex formation

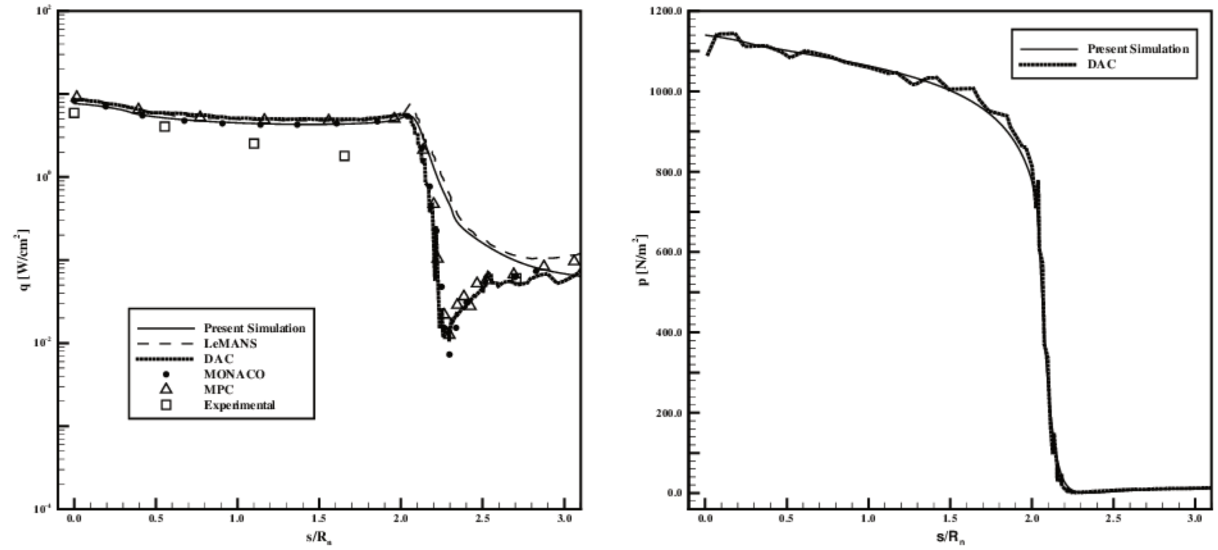

(a) Heat flux

(b) Pressure

Figure 6: Heat flux and pressure over the wall

layer because it is calculate from the temperature near to the wall and it is difficulty to measure precisely this property. Different modeling methods (RANS, DSMC) could bring different results in this region what need to be investigated the physics of the process. However, the pressure distribution is more related to the flow topology. As both results have similar streamlines pattern (Fig. 5), it is reasonable to have same results for pressure distribution, even though they have different formulation.

4.3 Case 2

The flow conditions in this case are more rarefied than case 3 as pointed by the global Knudsen number in Tab. 3. The local Knudsen number increases even more at expansion region at the back of the shoulder (Fig 2(a)). The present simulation did not show results good enough in the wake region, thus, only the front part of the probe was investigated. Since the flow is supersonic, the downstream perturbations do not interfere considerably on the flow characteristics upstream the computational domain was truncated at the probe shoulder as shown in Fig.1(b).

Figure 8 shows the streamlines, Mach number and temperature distribution contours for case 2. Similarly to case

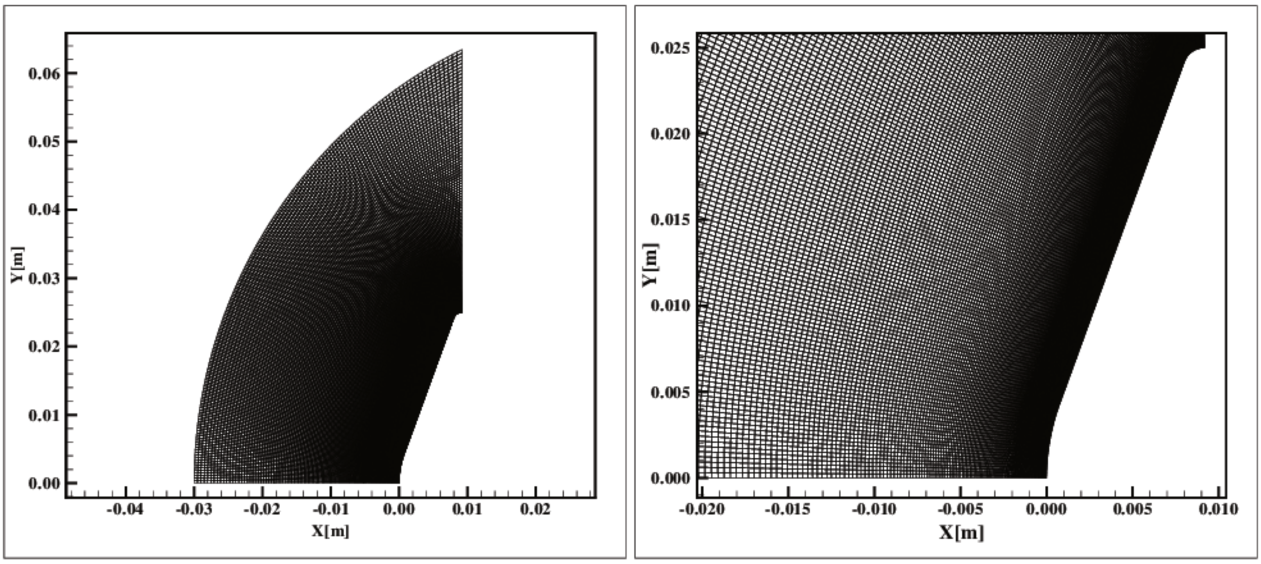

(a) Entire grid (b) Zoom

Figure 7: Computational grid for case 3

3, it is possible to see the shock wave structure and a smooth supersonic exit. The streamlines show the upstream flow coming parallel to the probe axis and changing direction after they pass through the shock wave. At the region close to the symmetry axis, the shock is near to normal and there is no significant change of direction. However, as it goes away from this region, the shock became oblique due to the probe geometry and the changing in the direction is more perceptible. This is confirmed by the oblique shock theory which was explained in case 3 whose results presented the same pattern (Fig. 4(a)).

Figure 9 show the computed heat flux and pressure over the probe wall. The heat flux results follow the same trend of the case 3 results: the present results have a good agreement when compared with other numerical results all predicts, approximately, the same heat flux peak. Furthermore, the experimental data is in good accordance with the simulated results. In the same way, the present simulation agrees with DAC results for the pressure over the probe wall. The reason for the good match between the results is the same as explained for the case 3 in the section 3.2.2..

Simulation properties extracted along line C1 (from Fig. 2(a)) are plotted in Fig. 10. As the C1 line passes (inward) through the shock it is noticed that the RANS codes have a density gradient higher than the DSMC codes (Fig. 10(a)). Away from the shock, the results agree among them. Figure 10(b) shows that the shock calculated by the DSMC codes is moved upstream in relation with the shock calculated by the RANS codes. In others words, the shock is closer to the wall for the RANS code. It is also important to say that the temperature peak in the shock is higher of the DSMC code rather the RANS code. The shock region has $Kn_{GL} > 0.1$ which implies a high degree of rarefaction of the flow and justifies the difference between the molecular and the continuum approach, which can not solve the flow with good accuracy. However, as the C1 get close to the wall and the local Knudsen number decreases, the results agree among them.

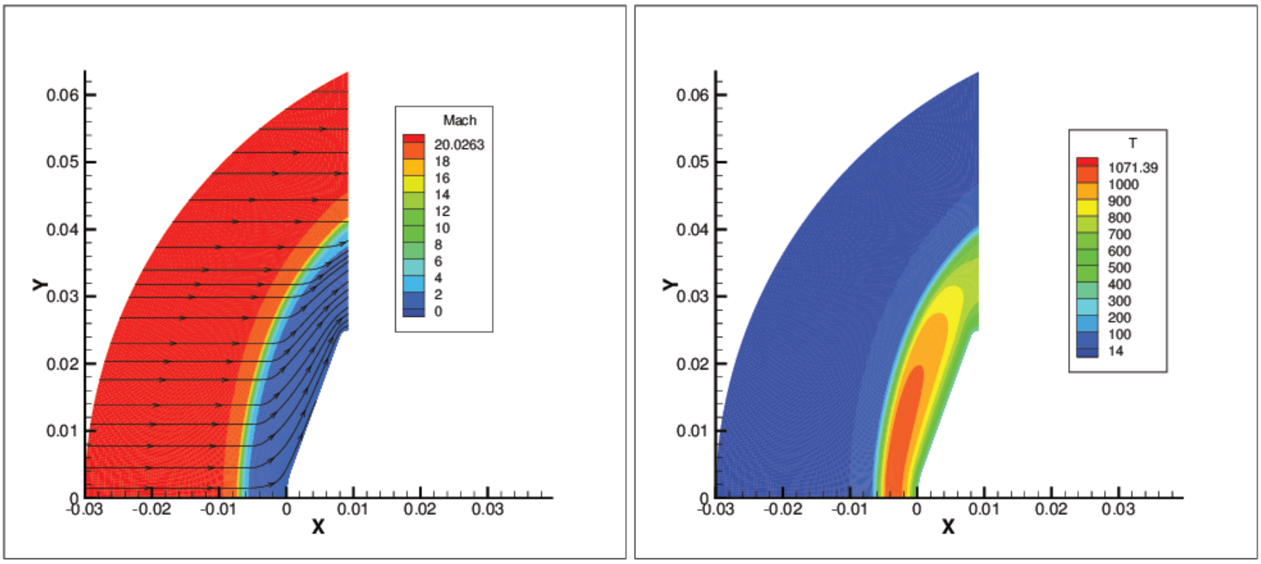

(a) Mach number (b) Temperature

Figure 8: Simulation results

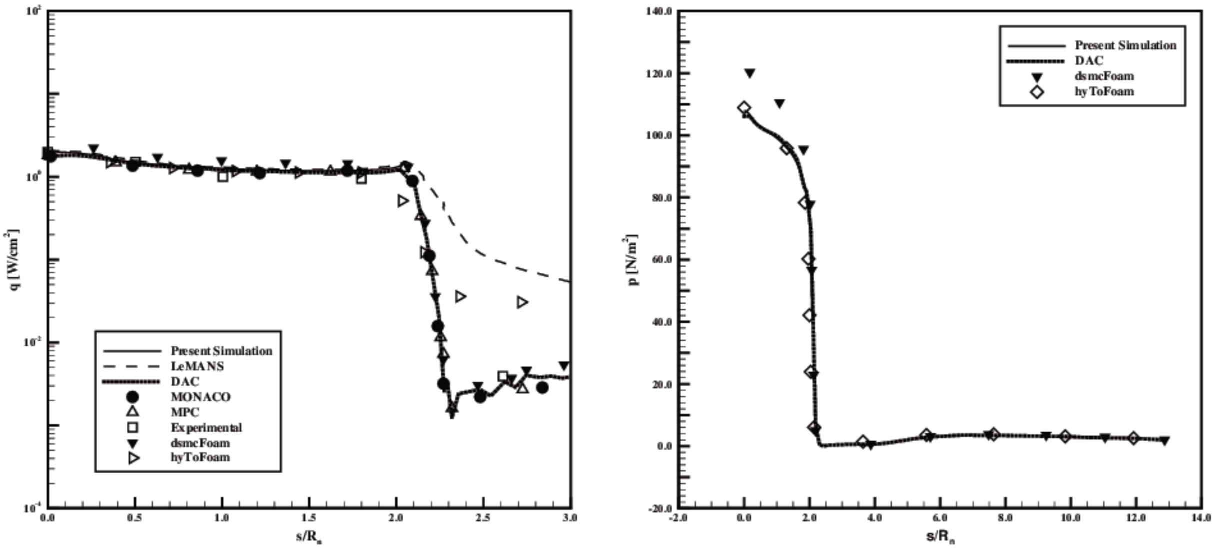

(a) Heat flux (b) Pressure

Figure 9: Heat flux and pressure over the wall

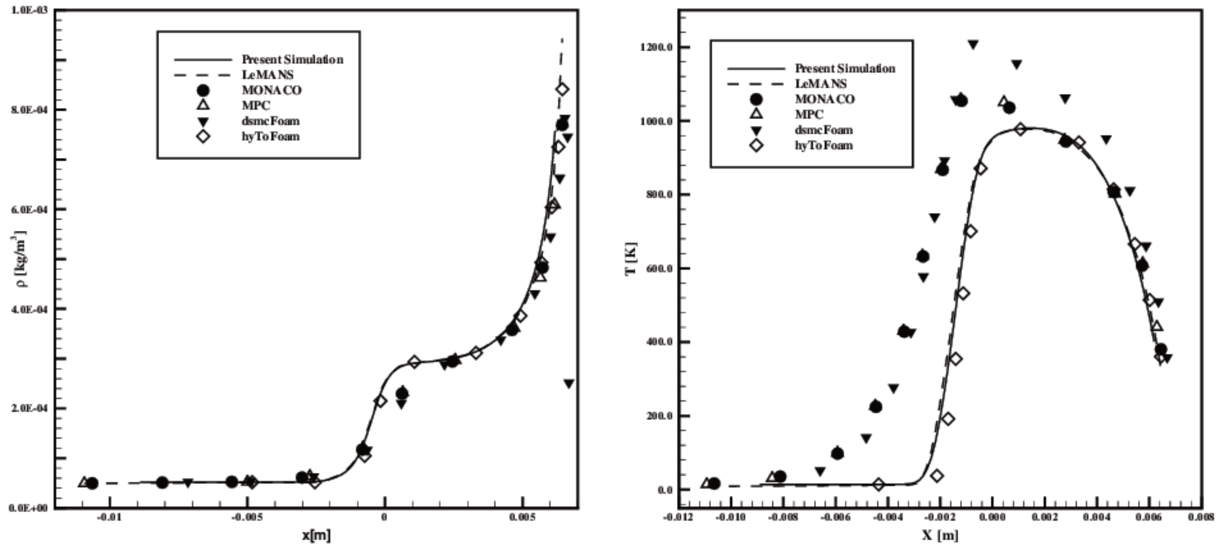

(a) Density (b) Temperature

Figure 10: Density and temperature over the C1 line

5. CONCLUSION

The present work compared the simulation results of the *in house* solver with experimental data and others solvers. In general, in the flow regions in which the local Knudsen number is grater than 0.1 the RANS solvers and the DSMC solvers disagree. This is expected because the continuum hypothesis is not assured for $Kn_{GL} > 0.1$ and the RANS results do not give the real physical meaning of the flow properties. Precisely, the transport properties are those in which loose more accuracy for this rarefied condition as seen in the heat flux results. In another way, the physical properties which are more related with flow topology, like pressure distribution, showed good agreement between the solvers.

Close of the heat shield planetary probe, it is observed that the flow properties results obtained by different approaches, RANS and DSMC, agree among them. In these region, the flow is considered continuous, corroborated by the local Knudsen number below 0.1, which allows the use of RANS formulation to calculate the flow properties around the frontal surface of the probe. Although the results at the wake region are no adequate, the main goal of the re-entry atmosphere vehicle simulation is to calculate the heat flux over the front part of the probe. Speaking about the aerospace vehicle project, the heat shield needs to be well designed to assure the protection of the vessel. Therefore, for practical purpose, the RANS approach could be used for heat shield design.

The next step in this work is to develop a hybrid CFD/DSMC code. i.e., for high local Knudsen number regions where the continuum formulation fail to give good results DSMC is employed and at the regions where low local Knudsen number is detected, RANS approach is used is used to speed up the code. At continuum regime DSMC method is very expensive due to the great number of particles required during the simulations.

6. ACKNOWLEDGEMENTS

The authors gratefully acknowledge the support for the present research provided by Conselho Nacional de Desenvolvimento Científico e Tecnológico, CNPq, under the Research Grants No. 309985/2013-7, No. 400844/2014-1 and No. 443839/2014-0. The work is also supported by Fundação de Amparo à Pesquisa do Estado de São Paulo, FAPESP, under Research Grants No. 2013/07375-0 and No. 2014/25438-1.

7. REFERENCES

Allegre, J., Bish, D. and Lengrand, J.C., 1997. "Experimental rarefied density flowfields at hypersonic conditions over 70-degree blunted cone". *Journal of Spacecraft and Rockets*, Vol. 34, pp. 714–718.

Bird, G.A., 1994. *Molecular Gas Dynamics and the Direct Simulation of Gas Flows*. Oxford Science Publications.

Moss, J.N., Dogra, V.K. and Wilmoth, R.G., 1993. "Dsmc simulations of mach 20 nitrogen flows about a 70 deg. blunted cone and its wake". Nasa technical memorandum, National Aeronautics and Space Administration, Hampton, Virginia.

Scalabrin, L.C., 2007. *Multiscale Particle-Continuum Simulations of Hypersonic Flow over a Planetary Probe*. Ph.D. thesis, The University of Michigan.

Schwartzentruber, T.E., Scalabrin, L.C. and Boyd, I.D., 2008. "Multiscale particle-continuum simulations of hypersonic flow over a planetary probe". *Journal of Spacecraft and Rockets*, Vol. 45, pp. 1196–1206.

8. RESPONSIBILITY NOTICE

The following text, properly adapted to the number of authors, must be included in the last section of the paper: The authors are the only responsible for the printed material included in this paper.